Chinese Chemical Letters 35 (2024) 108451

Contents lists available at ScienceDirect

Chinese Chemical Letters

journal homepage: www.elsevier.com/locate/cclet

Congener-derived template to construct lithiophilic organic-inorganic layer/interphase for high volumetric capacity dendrite-free Li metal batteries

Kang Yang, Long Li, Yuanbin Xiao, Qiaoli Zhang, Chenpeng Xi, Borong Li, Yan Yu*, Chengkai Yang*

Key Laboratory of Advanced Materials Technologies, International (HongKong Macao and Taiwan) Joint Laboratory on Advanced Materials Technologies, College of Materials Science and Engineering, Fuzhou University, Fuzhou 350108, China

ARTICLE INFO

Article history:
Received 10 February 2023
Revised 13 March 2023
Accepted 12 April 2023
Available online 13 April 2023

Keywords:
Lithium metal anode
Congener-derived
Lithiophilicity
Volumetric capacity
Organic-inorganic interphase

ABSTRACT

The development of lithium-metal batteries (LMBs) is seriously restricted by the out-of-control dendrites growth and infinite volume expansion. Herein, a pervasive organic-inorganic layer construction strategy is reported for the composite lithium metal anode with congener-derived organic-inorganic solid electrolyte interphase (SEI). In this strategy, the organic-inorganic Ag@polydopamine (Ag@PDA) layer is coated on the arbitrary substrates by a simple two-step method. The thin and stable congener-derived SEI is *in-situ* formed with fewer inorganic components and more organic components during charging/discharging. The polydopamine with sufficient adhesion groups and lithiophilic Ag layer realize near-zero nucleation overpotential during lithium deposition. The low interface resistance and stable lithium deposition are achieved. Moreover, the practical areal and volumetric capacities of the composite anode with three-dimensional copper (3DCu) as the substrate are 10 mAh/cm^2 and 1538 mAh/cm^3 (*vs.* the mass of anode). The symmetrical cell shows very low polarization voltage (10 mV) and more than 2500 h cycles life at 1 mA/cm^2 (1 mAh/cm^2). The $LiNi_{0.8}Co_{0.1}Mn_{0.1}O_2$ (NCM811)-based full cells show improved capacity retention (82%) after 100 cycles at 0.5 C. The modified lithiophilic anode with congener-derived interphase provides a promising strategy to realize the next-generation dendrite-free LMBs.

Rechargeable batteries with high energy density and long cycle life are essential for portable electronic devices, electric vehicles, and large-scale energy storage systems [1,2]. In recent years, lithium-ion batteries based on graphite anode have found it increasingly difficult in meeting the higher energy density demand [3,4]. Intensive research on lithium metal batteries (LMBs), including lithium-sulfur, lithium-air, and lithium metal *versus* intercalation-type cathodes [5–7], are enthusiastically pursued. LMBs have been widely studied because of lithium's ultra-high volumetric capacity (2061 mAh/cm^3, three times the graphite of 719 mAh/cm^3) and extremely negative redox potential (−3.04 V *vs.* SHE) [8]. However, the practical application of rechargeable LMBs are still hindered by two main problems. First, as a kind of "non-host" anode, the plating/stripping process of lithium will probably involve dramatic changes [9–11], such as uneven volume change and the exposed fresh lithium metal, resulting in a low coulombic efficiency [12–14]. The uneven lithium deposition leads to the formation of tip protuberances, causing internal short circuits and severe safety risks [15,16].

To solve these problems, many strategies have been proposed to inhibit dendrite growth and stabilize solid electrolyte interphase (SEI) [17,18]. It can be roughly divided into the following types: (1) The construction of higher mechanical modulus and stable coatings on lithium anodes [19–24]; (2) effective electrolyte additives to build a stable SEI away from irreversible reactions with organic electrolytes [25,26]; (3) solid and gel electrolytes with high shear modulus inhibit the dendrite's growth [27,28]; (4) constructing 3D current collector according to the "sand" time model [29–32]. However, because of the poor lithiophilicity and unstable SEI of most collectors, it is still challenging to achieve a uniform deposition into the 3D structure without dendrites [33]. There have been some previous works to modify current collectors with inorganic or organic compounds while most anodes are difficult to cope with the huge volume changes under long cycles and have great limitations in practical applications [34–36].

Incorporating organic-inorganic SEI onto a modified anode to build congeneric organic-inorganic composite interphase/layers

* Corresponding authors.
E-mail addresses: yuyan@fzu.edu.cn (Y. Yu), chengkai_yang@fzu.edu.cn (C. Yang).

https://doi.org/10.1016/j.cclet.2023.108451
1001-8417/

could combine the merits of both the individual components and provides stable performance. This strategy enables the simultaneous formation of a compatible organic-inorganic composite anode layer with its congeneric organic-inorganic interphase, which is in situ formed during charging/discharging. Unfortunately, the organic-inorganic composite interphase is prone to phase separation which results in inhomogeneous deposition and low coulombic efficiency owing to the inherently poor compatibility of inorganic layers with organic materials. Therefore, a pre-existing lithium plating framework with its congener-derived SEI is highly desirable and necessary for obtaining high capacity and long-life LMBs.

Here, a strategy of incorporating versatile organic-inorganic layers with reversible lithiophilicity and congener-derived SEI is designed. The PDA as the organic layer with abundant *o*–dione that can adsorb Li^+ and assist in the deposition. The Ag particles as the inorganic layer can form Ag-Li alloy with Li to significantly reduce the nucleation overpotential. After the initial lithium deposition, the Li-Ag alloy is electrochemically formed on the surface, forming a kind of congener-derived SEI with minor inorganic components and more organic components. The effectiveness of this strategy is verified on three-dimensional copper (3DCu) and porous carbon skeleton (PCS) substrate respectively. Notably, this strategy for preparing congener-derived templates is easy to put into the manufacture and extended to other substrate materials.

Referring to the previous work [37–40], we adopt a simple and low-cost strategy. First, the commercial H62 brass sheet (composed of Cu and Zn with a mass ratio of 65:35) was cut into flakes, and the surface oil and impurities were removed by ultrasonic cleaning with acetone and ethanol, then it was soaked in 3 mol/L hydrochloric acid (HCl) + 5 mol/L ammonium chloride (NH_4Cl) and heated in a water bath at 80 °C. In this process, the Zn element was preferentially removed, and the 3DCu structure with a high specific surface area was obtained. Then used 0.01 mol/L trimethylol aminomethane and 0.01 mol/L HCl to configure the Tris–HCl buffer solution (pH 8.5), Subsequently, dopamine hydrochloride at a concentration of 2 g/L was dissolved in it. Afterwards, the 3DCu was immersed in the above-mentioned solution and heated at 40 °C for 20 h, during which dopamine will be self-polymerized and coated on the 3DCu surface. Then, under the condition of magnetic stirring, the ammonia of 1 mol/L was added to the $AgNO_3$ solution with the concentration of 0.005 mol/L until the precipitation was just dissolved to obtain the Ag ammonia solution, in which the 3DCu coated with polydopamine (PDA@3DCu) was immersed in the Ag ammonia solution and subjected to a 60 °C water bath for 10 min. After the completion of the reaction, Ag particles were attached to the surface to obtain Ag@PDA@3DCu. In addition, The Ag@PDA@3DCu-Li anode had a thickness of 65 μm after preloading lithium 10 mAh/cm^2 (Fig. S1a in Supporting information).

The preparation process of PCS involved the carbonization of rice paper film in a tube furnace at 500–800 °C for 2 h. The subsequent coating process of the Ag@PDA layer was the same as Ag@PDA@3DCu. In addition, Fig. S1b (Supporting information) showed the Ag@PDA@PCS-Li anode had a thickness of 83 μm after preloading lithium 10 mAh/cm^2, Its mass is only 8.4 mg, therefore, it also has a higher volume-specific capacity.

The morphology, pore size, microstructure, and element distribution of Ag@PDA@3DCu and Ag@PDA@PCS samples were observed by scanning electron microscope (SEM, Helios G4 CX) and energy dispersive spectroscopy (Helios G4/EDS). The FTIR spectrophotometer (Nicolet 5700) was used to characterize the chemical structure of the introduced PDA layer. X-ray photoelectron spectroscopy (XPS) measurements were performed on a Thermo ESCALAB 250 spectrometer, using non-monochromatic Al Kα X-rays as the excitation source and choosing C 1s (284.8 eV) as the reference line.

To evaluate the electrochemical performance of half-cells and Li-Li symmetrical cells, the CR2032 coin cell was assembled, Celgard2400 microporous polypropylene film as separator, and 1 mol/L LiTFSI in cosolvent of 1,3-dioxolane (DOL) and 1,2-dimethoxyethane (DME) (1:1, v/v) with 1 wt% $LiNO_3$ as the electrolyte solution. These cells were assembled in an argon-filled glove box. The assembled half-cells were prepared with various substrates as working electrodes and Li as the counter electrode. To test the nucleation overpotential, 1 mAh/cm^2 of Li was deposited at 0.5 mA/cm^2. To test CE, a fixed amount of Li of 1 mAh/cm^2 was deposited at 0.5 mA/cm^2 and 1 mA/cm^2, then stripped to 1 V in each cycle. Electrochemical impedance spectroscopy (EIS) measurements using CHI660e electrochemical station in the frequency range from 100 kHz to 10 mHz. Before assembling the symmetrical cell, the selected substrates (2DCu, 3DCu, PDA@3DCu, Ag@3DCu, Ag@PDA@3DCu and Ag@PDA@PCS) were deposited with a capacity of 10 mAh/cm^2 at a current density of 0.5 mA/cm^2. Then, the cells were disassembled and the composite anodes were washed with DOL. In the full-cell experiment, the slurry was prepared by mixing $LiFePO_4$ (LFP), conductive carbon additives, and polyvinylidene fluoride (PVDF) into *N*-methyl pyrrolidone (NMP) at an 8:1:1 mass ratio. Then, the paste was coated on aluminum foil, and the electrode was dried overnight in a vacuum at 120 °C. The mass loading is about 4 mg. Similarly, $LiNi_{0.8}Co_{0.1}Mn_{0.1}O_2$ (NCM811) was prepared by mixing NCM811, conductive carbon additives, and polyvinylidene fluoride (PVDF) into *N*-methyl pyrrolidone (NMP) at 18:1:1 mass ratio, the mass loading is about 6 mg. The electrolyte used in the full cell test was 1.0 mol/L $LiPF_6$ in EC/DMC/EMC (1:1:1, v/v/v) with 5% FEC. When equipped with LFP cathode. The full cells were cycled between 2.8 V and 4.2 V. When equipped with NCM811 cathode, the operating voltage range of the full cells is 2.8–4.3 V.

All calculations were performed by using the projector augmented wave method in the framework of the density functional theory (DFT), as implemented in the Vienna ab-initio Simulation Package (VASP), and the results were visualized in VESTA. In DFT calculations, the Generalized gradient approximation (GGA) and Per-dew–Burke–Ernzerhof (PBE) exchange function were used. The plane-wave energy Cut-off was set to 520 eV, and the k-point mesh of $3 \times 3 \times 1$ in the Gamma-centered grids for the structural relaxation. To explore the interactions between Li atom and Cu (111), Ag (111), PDA, and Ag@PDA, the adsorption energies of one Li atom on the substrate surfaces were calculated. A vacuum region of 15 Å was applied to avoid interactions between the neighboring configurations. The binding energy (E_b) was calculated by the energy difference of the system after and before the adsorption:

$$E_b = E_{total} - E_{sub} - E_{Li} \quad (1)$$

where E_{total}, E_{Li} and E_{sub} represent the DFT energies of the Li adsorbed substrate, the energy of an isolated Li atom, and the energy of the substrate, respectively.

Fig. 1 shows the schematic of the process for Ag@PDA@arbitrary substrates and its congener-derived SEI. As shown in Fig. 1a, several typical structures such as 3DCu, PCS, and other matrices are coated with the Ag@PDA layer, obtaining stable congener-derived SEI after lithium deposition. The strategy is first validated on 3DCu, the 40 μm thickness brass sheet is dealloyed in dilute hydrochloric acid. Fig. 1b shows the 3DCu with pore diameters from 200 nm to 2 μm. Fig. 1c shows the polydopamine (PDA) firmly adheres to the 3DCu substrate. In Figs. 1d and e, the Ag nanoparticles are reduced on PDA@3DCu substrates by Ag mirror reaction evenly. The size of Ag particles is around 30–100 nm. Figs. 1f-i show the distribution of the three elements Cu, Ag and C, The total spectrum of the element distribution map in Fig. S2 (Supporting information) shows that the Zn element is completely removed. Here, the polydopamine is used as a reducing agent to slowly reduce Ag^+ and

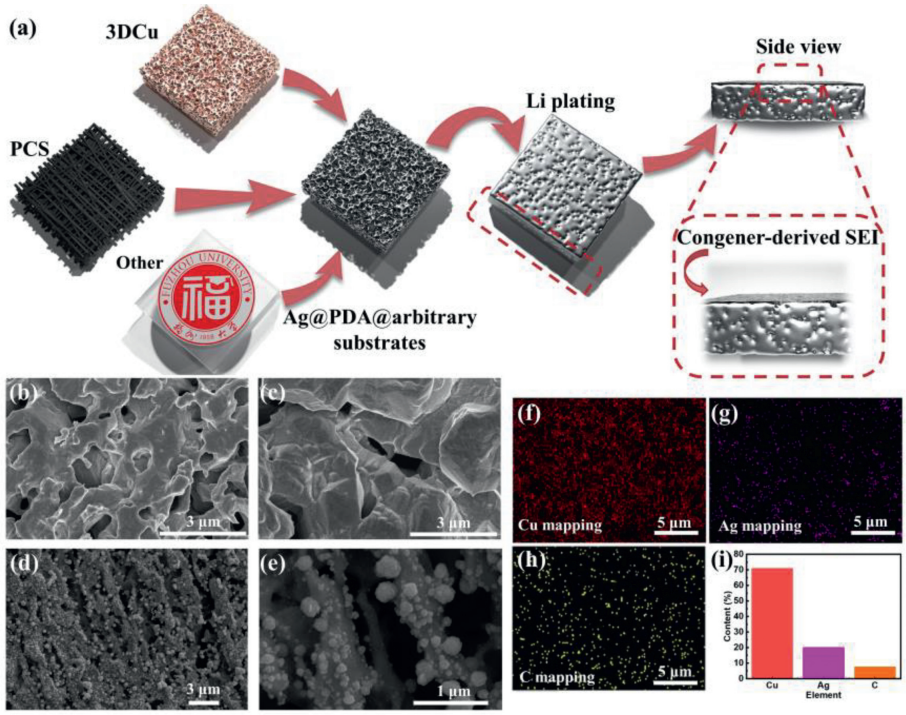

Fig. 1. (a) Schematic diagram of Ag@PDA@arbitrary substrates and its congener-derived SEI. SEM images of (b) 3DCu, (c) PDA@3DCu, (d, e) Ag@PDA@3DCu. (f-i) Element mapping and proportion of the Cu Ag and C.

adhere to the substrate. Without this polydopamine layer, Ag crystals will quickly grow in the form of dendrites on the 3DCu (Fig. S3 in Supporting information). Fourier transform infrared spectroscopy (FTIR) proved that PDA still exists after the introduction of Ag particles (Fig. S4 in Supporting information), the FTIR spectra of PDA@3DCu is similar to Ag@PDA@3DCu, the absorption peak at 3425 cm^{-1} is ascribed to O–H/N–H stretching vibrations between PDA molecules, the peaks at 2930 cm^{-1} and 2850 cm^{-1} are attributed to the C–H stretching vibration, the peak at 1630 cm^{-1} is the overlapping peak of C=C stretching vibration and N–H bending vibration on the benzene ring, the peak at 1050 cm^{-1} is attributed to C–N stretching vibration. The above results prove that the Ag@PDA layer is successfully coated on the 3DCu substrate.

To further study the surface and SEI composition after cycling, the anodes were analyzed after 20 cycles by XPS spectrum. There are four peaks in the C 1s spectrum at 289.8, 288.83, 286.36 and 284.8 eV, corresponding to Li_2CO_3, C=O, C–O, and C–C (Figs. 2a and e). F 1s spectrum shows two peaks in 688.6 eV and 684.9 eV, corresponding to C–F and LiF, respectively (Figs. 2b and f). Li 1s spectrum has three peaks at 55.6, 55.2 and 54.7 eV, corresponding to LiF, Li_2CO_3, and C–O–Li (Figs. 2c and g). The O 1s spectrum shows three peaks at 532.7, 531.7 and 531.08 eV, corresponding to C–O, C=O and C–O–Li, respectively (Figs. 2d and h). These results show that the composition of SEI mainly comes from the decomposition of electrolytes. The main components of SEI are listed in Fig. 2i with the proportion of each component. By comparison, the inorganic components such as Li_2CO_3 and LiF on the surface of Ag@PDA@3DCu are significantly less than those of ordinary Cu foil. The proportion of organic components such as C–O–Li is relatively higher. In addition, the full spectrum of XPS and the ratio of each element are shown in Fig. S5 (Supporting information). The lower ratio of Li element on the surface of Ag@PDA@3DCu also proves that it has higher Coulombic efficiency, and the deposited Li can be stripped to a greater extent. The amount of participation in the formation of SEI and "dead lithium" is very small. The characteristic peaks of N and S signals were provided in Fig. S6 (Supporting information), and the weakening of the peak intensity of the inorganic component $LiNO_2$ was also observed. This shows fewer inorganic components and more organic components, forming a thin and flexible SEI on the Ag@PDA@3DCu after many cycles. A reasonable amount of inorganic components could enhance and stabilize the SEI layer, while too many inorganic components make the deposition of lithium ions more inhomogeneous. The stable congener-derived layer/interphase contains rigid inorganic components and flexible organic components, which provide flexibility and elasticity to stabilize the lithium metal anode during cycling. In order to explore nucleation characteristics of the congener-derived anode, the nucleation and growth model were explored in the symmetrical cell at a constant potential at −0.3 V. From the time-current curve in Fig. 2j, the time corresponding to the maximum point here is t_m (relaxation time), and the corresponding peak current is i_m (current caused by the nucleation process) [41], In this test, The t_m of Ag@PDA@3DCu-Li is smaller than Li, which proves the relaxation time is shorter, and the i_m of Ag@PDA@3DCu-Li is larger, indicating the growth rate of crystal nucleus is faster. The $t_m i_m^2$ is positively correlated with the number of crystal nucleation [42,43], it is proved that the number of crystal nucleation on the Ag@PDA@3DCu-Li is much higher. Fig. S7 (Supporting information) shows the description of the classical nucleation theory for instantaneous nucleation and progressive nucleation. The normalized curve in Fig. 2k shows that both of them follow an instantaneous nucleation model compared to the standard nucleation curve. However, in the formation stage of SEI, the nucleation curve of lithium deviates from the standard curve earlier and continues to be higher than Ag@PDA@3DCu-Li. Thus, the side reactions in SEI continue to take place on the surface of Li, bringing more by-products such as Li_2CO_3, while Ag@PDA@3DCu-Li significantly inhibits this process due to the stable congener-derived SEI.

In order to further explore the lithiophilicity of the congener-derived template. 2DCu, 3DCu, and Ag@PDA@3DCu were used to assemble coin cells. At 0.5 mA/cm^2, their nucleation overpoten-

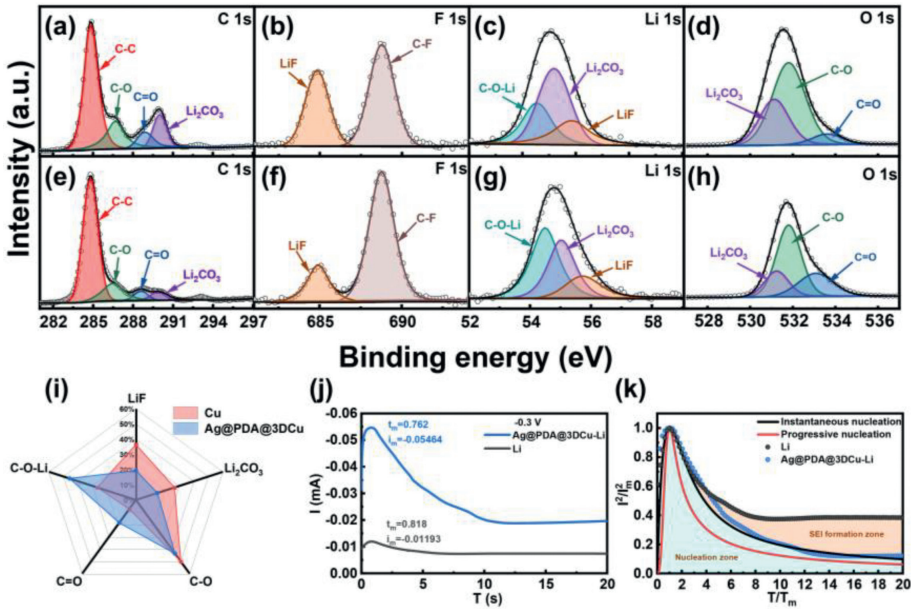

Fig. 2. X-ray photoelectron spectroscopy (XPS) analysis of (a, e) C 1s, (b, f) F 1s, (c, g) Li 1s, (d, h) O 1s for lithium plating/stripping on Cu and Ag@PDA@3DCu after 20 cycles. (i) Distribution map of various components in SEI. Ag@PDA@3DCu-Li and Li were deposited at constant potential to obtain (j) current-time curve and (k) normalized curve.

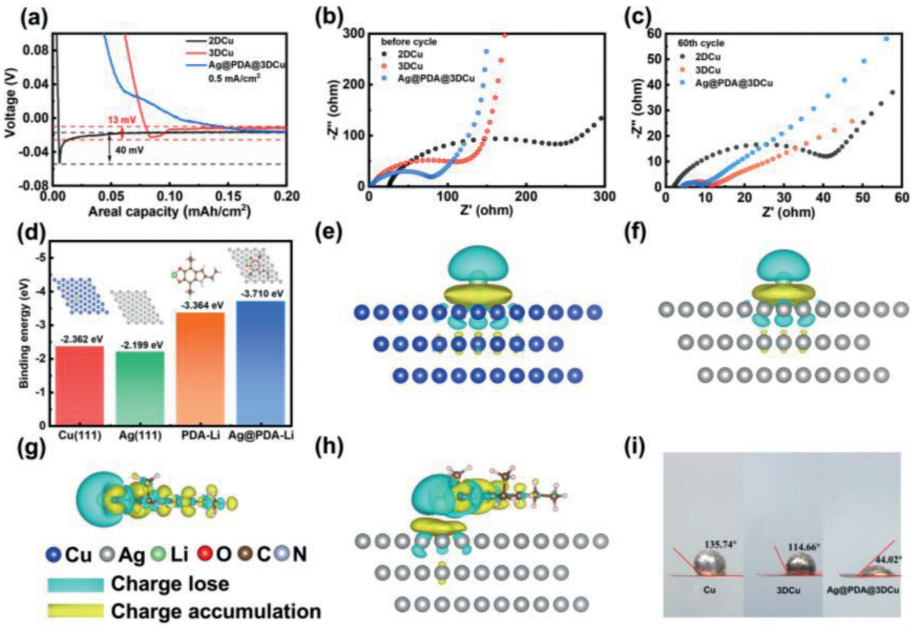

Fig. 3. (a) Constant current curves of the Li plating on the 2DCu, 3DCu and Ag@PDA@3DCu at 0.5 mA/cm^2. (b, c) Electrochemical impedance before and after cycle. (d) Summary of the calculated binding energy of Li atom with Cu, Ag, PDA and Ag@PDA surface. The charge density differences with one Li atom adsorbed on the (e) Cu, (f) Ag, (g) PDA, (h) Ag@PDA. The isosurface value is set to 0.0008 bohr^{-3}. (i) The molten lithium photos of contact angle for 2DCu, 3DCu and Ag@PDA@3DCu.

tial is studied in Fig. 3a. The overpotential of lithium deposition on 2DCu is 40 mV, while 3DCu is 13 mV. The Ag@PDA@3DCu shows nearly zero nucleation overpotential, which means an improved lithiophilicity and reduced nucleation barrier. Electrochemical impedance spectroscopy (EIS) of the cells with different current collectors was determined to investigate the interfacial stability in Figs. 3b and c. The charge transfer resistance of 2DCu and 3DCu electrodes before cycling are 251.2 Ω and 127.4 Ω, respectively. The Ag@PDA@3DCu has the lowest charge transfer resistance of 78.52 Ω. After 60th cycles, the Ag@PDA@3DCu electrode maintains the lowest R_{sei} of 5.063 Ω, while the R_{sei} of 3DCu and 2DCu electrodes after 60 cycles is 6.54 Ω and 38.706 Ω, respectively. The results indicate that the introduced congener-derived layer/interphase is beneficial to the redox reactions and promote the process of charge transfer.

To further understand the function of each component in Ag@PDA@3DCu, the density functional theory (DFT) calculations were carried out. Referred to the previous work [44,45], The 5,6-indolequinone was studied as a typical structure after oxidation of PDA, the binding energies and charge density differences of lithium atom on Cu, Ag, PDA, and Ag@PDA substrates were calculated respectively. The several adsorption sites of Li on PDA are all shown in Fig. S8 (Supporting information). The lithium atom has the strongest binding energy near the carbonyl group. In Fig. 3d, the Ag@PDA composite structure shows the lowest binding energy for lithium with the auxiliary PDA. The results indicate that the

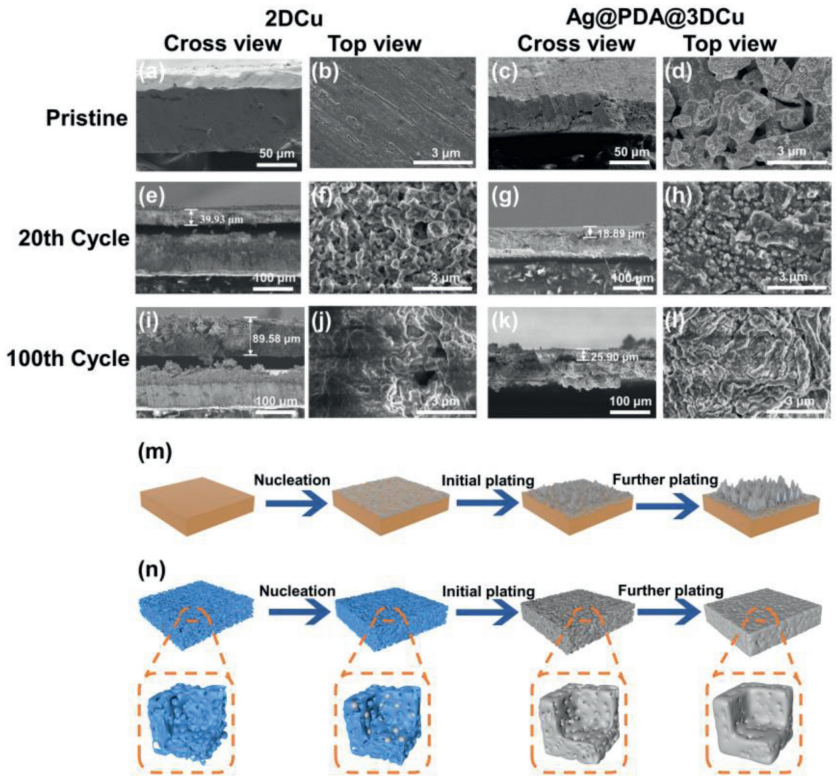

Fig. 4. SEM images of the morphology of Li deposited at 1 mA/cm^2 (1 mAh/cm^2): (a, e, i) Cross-sectional SEM images of 2DCu at the pristine state, the 20th cycle, and the 100th cycle. (b, f, j) Top-view SEM images of the 2DCu at the pristine state, the 20th cycle, and the 100th cycle. (c, g, k) Cross-sectional SEM images of Ag@PDA@3DCu at the pristine state, the 20th cycle, and the 100th cycle. (d, h, l) Top-view SEM images of the Ag@PDA@3DCu at the pristine state, the 20th cycle, and the 100th cycle. Schematic illustration of Li deposition behavior on (m) 2DCu and (n) Ag@PDA@3DCu substrates.

lithium atom is preferentially adsorbed and complexed with the o–dione of groups on the Ag@PDA structure. Thus, the Ag@PDA layer can induce preferential adsorption and reduction, and further form Ag-Li alloy, which effectively reduces the nucleation barrier and promotes the uniform deposition of lithium. Since the deposition morphology is closely related to the charge distribution on the substrate surface, Figs. 3e-h show the charge density difference diagram of the above four models. When lithium is deposited on surfaces, the electrons near the deposition site tend to be concentrated, resulting in non-uniform lithium deposition. For the Ag@PDA, the interaction between Li^+ and PDA induces uniform charge distribution, lithium deposition, and uniform Li^+ flux. Thus, the Li^+ in the electrolyte would not accumulate. This result proves the improvement of the surface affinity of the accumulate easily layer. Fig. 3i shows that molten lithium exhibits the smallest contact angle on Ag@PDA@3DCu, which further demonstrates its excellent wettability and the reduced nucleation barrier.

The congener-derived template was conducive to inhibiting the side reactions, which was consistent with the thinner dead lithium and fewer by-product layers observed in Fig. 4. The morphology evolution is studied at different cycles at 1 mA/cm^2 (1 mAh/cm^2). On the 2DCu, the thickness of deposited lithium increased from 39.93 μm to 89.58 μm during 20–100 cycles, and its structure became looser. This loose structure consists of moss-like lithium and dead lithium (Figs. 4e and i), which further aggravates the uneven growth of lithium. The plating/stripping of lithium on Ag@PDA@3DCu is smoother and more stable. With the cycle increased, the thickness of the lithium increased from 18.89 μm to 25.9 μm (Figs. 4g and k), which indicates that the porous structure accommodates the volume expansion and the Ag nanoparticles promote the reversibility of Li-plating/stripping. In addition, according to the top view, the surface of the 2DCu becomes quite loose after a long cycle, and much spherical lithium accumulates on the surface after 100 cycles, indicating dendrites growth in the subsequent cycle (Figs. 4f and j). The morphology deposited on Ag@PDA@3DCu was significantly improved (Figs. 4h and l).

To further explore the nucleation behavior, the Ag@PDA@3DCu with an ultra-smooth lithium plating/stripping process is observed at 1 mA/cm^2 in Fig. S9 (Supporting information). First, the 2, 4, 6, 8 and 10 mAh/cm^2 lithium was deposited, and then it was stripped in turn. In process of plating, lithium is limited in the 3D structure; original pores are gradually filled, and the stripping process can maintain stability. The discharge and charging curves show a stable voltage platform, which means a stable electrochemical surface during the cycle. Therefore, the porous Ag@PDA@3DCu can be used as a robust framework for lithium deposition. On this basis, dendrite puncture experiments were performed in Fig. S10 (Supporting information). At 2 mA/cm^2, the cell with 2DCu and 3DCu suddenly shorted at about 45 h and 32 h, respectively. However, the cell with Ag@PDA@3DCu does not have a short circuit until the lithium is exhausted.

This phenomenon is consistent with our preconceived mechanism (Figs. 4m and n). When lithium is deposited on 2DCu, the current is accumulated at the protuberances, further accelerating the dendrite's growth, as well as the fracture and regeneration of SEI. Different from the vertical growth, lithium gradually fills the pores and forms smooth Li layers and stable SEI due to the guidance on the congener-derived template.

To further investigate the potential of the Ag@PDA@3DCu for practical applications, coulombic efficiency was measured by plating 1 mAh/cm^2 Li at different current densities and then charging up to 1 V (*vs.* Li^+/Li) for cycles (Figs. 5a and b). Benefiting from the better congener-derived surface, the Ag@PDA@3DCu can be enhanced to 480 stable cycles and maintain a coulombic effi-

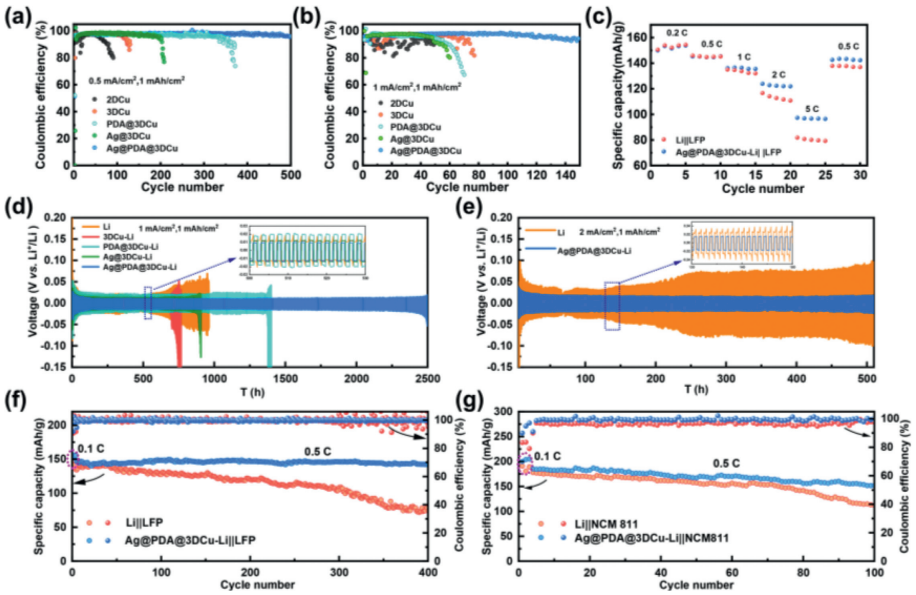

Fig. 5. Coulombic efficiency of Li plating/stripping on 2DCu, 3Dcu, PDA@3DCu, Ag@3DCu and Ag@PDA@3DCu at (a) 0.5 mA/cm^2 and (b) 1 mA/cm^2. (c) Rate performance of Ag@PDA@3DCu-Li||LFP and Li||LFP full cells. Voltage profiles of Li plating/stripping in symmetric cells with Li, 3DCu-Li, PDA@3DCu-Li, Ag@3DCu-Li and Ag@PDA@3DCu-Li electrodes cycled at (d) 1 mA/cm^2 (1 mAh/cm^2) and (e) 2 mA/cm^2 (1 mAh/cm^2). Long-term cycling performance of full cells with (f) LFP and (g) NCM811 at 0.5 C.

ciency of more than 96%. In contrast, the CE of the PDA@3DCu drops below 90% after 300 cycles due to the reversibility of PDA is slightly worse. the CE of the Ag@3DCu decreases to less than 90% after 170 cycles due to the Ag dendrites blocking the pores of 3DCu and making it lose its host role, Cu and 3DCu lose their usefulness faster due to their poor lithiophilicity and uneven lithium deposition behavior. With increasing current density to 1 mA/cm^2, Ag@PDA@3DCu still exhibits a highly stable CE. To emphasize the importance of Ag@PDA@3DCu-Li composite anode after preloading lithium, the rate performance was tested with the cathode of LFP. It can be seen from Fig. 5c that the anode of Ag@PDA@3DCu-Li showed higher discharge capacity and had advantages even at a higher rate. To further study the long-term stability of the Ag@PDA@3DCu-Li, symmetric cells were assembled and then cycled under 1 mA/cm^2 (1 mAh/cm^2). As shown in Fig. 5d, Ag@PDA@3DCu-Li shows a 30 mV overpotential at the beginning of the cycle and decreases to 10 mV after 50 cycles and maintains 2400 h, the other groups all failed in a shorter time due to poor interfacial reaction and rapid consumption of electrolyte, it can be seen from the detailed diagram that Ag@PDA@3DCu-Li has the lowest overpotential, indicating that its congener-derived interface is more favorable for lithium deposition. With increasing current density to 2 mA/cm^2, as shown in Fig. 5e, Ag@PDA@3DCu-Li is able to maintain 15 mV and cycle stably more than 500 h, while the polarization voltage of Li foil starts to increase sharply from 200 h (greater than 70 mV). To further verify the applicability of the composite anode under higher current and capacity, we tested the symmetrical cells with 2 mA/cm^2 (2 mAh/cm^2) and 5 mA/cm^2 (2 mAh/cm^2). As shown in Fig. S11 (Supporting information), both of them can run smoothly at a lower polarization voltage, showing their potential to operate at high rates.

After that, using LFP and NCM811 as cathodes to assemble the full cells to evaluate the cycle stability of composite anode in practical application. Fig. 5f shows the discharge capacity of full cells using Li as the anode is about 144.75 mAh/g at the first cycle and decays rapidly in 400 cycles (0.5 C), by contrast, cells with Ag@PDA@3DCu-Li anode exhibit the much higher initial capacity of 154.4 mAh/g and improved capacity retention (97%) with a capacity of 142.3 mAh/g after 400 cycles. From the voltage-specific capacity curve of the corresponding charge-discharge process shown in Fig. S12 (Supporting information), from the 1st to the 400th cycle, the full cell with Ag@PDA@3DCu-Li as the anode shows better cycle stability and the polarization voltage is much lower than the cell with Li anode, which indicates that the reduction of interfacial side reactions and favors to efficient Li^+ transport. Fig. S13 (Supporting information) shows the outstanding performance of Ag@PDA@3DCu-Li||LFP at 1 C and 2 C. Further using NCM811 as the cathode to assemble the full cells, the Ag@PDA@3DCu-Li||NCM811 cell exhibits a high initial discharge capacity of 200.1 mAh/g, and a high capacity retention rate of 82% after 100 cycles at 0.5 C, which is higher than Li||NCM811 cells with a capacity retention rate of 64.8% (Fig. 5g).

To further study the applicability of this strategy on other matrices, commercial rice paper films were carbonized at high temperature, and the prepared porous carbon structure (PCS) was directly used as a carrier for the modification of organic-inorganic interphase layers. Fig. 6a shows the preparation process of the Ag@PDA@PCS-Li composite anode and its corresponding morphology at each stage. The pore size range of PCS is 10–30 μm, which is much larger than that of 3DCu, implying a larger lithium storage capacity. After preloading lithium, the original pores are filled, and a lithium composite anode with a very flat and dense surface is obtained. Fig. S14 (Supporting information) demonstrates the excellent stability of Li plating and stripping on Ag@PDA@PCS during continuous cycling. Figs. 6b and c show the symmetric cell performance at 1 mA/cm^2 and 2 mA/cm^2. The Ag@PDA@PCS-Li maintains an ultra-low polarization at 10 mV for 2800 h compared to the higher polarization of the control group. Even if the current increases to 2 mA/cm^2, it still maintains a low polarization for over 1800 h. Fig. 6d shows the performance of two anodes assembled with LFP cathodes at 0.5 C for 500 cycles with almost 100% capacity retention. Further assembly of the full cells with NCM811 as cathode shows that the Ag@PDA@PCS-Li||NCM811 cell exhibits a higher initial discharge capacity of 199.8 mAh/g and a higher capacity retention rate of 86.2% after 100 cycles at 0.5 C compared to the Li||NCM811 cell (Fig. 6e). This means the congener-derived interphase/layer is also applicable and had an outstanding performance on PCS. Thus, this strategy is a templated approach that could be applied at any scale. Fig. S15 (Supporting information)

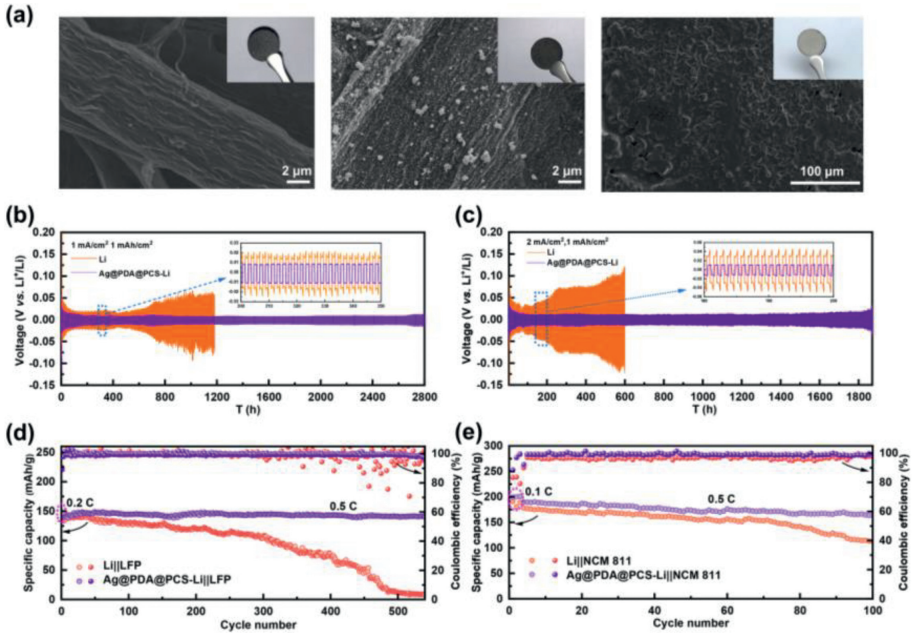

Fig. 6. SEM images and top view photos of lithium composite anodes. (a) From left to right are PCS, Ag@PDA@PCS, Ag@PDA@PCS-Li. Voltage profiles of Li plating/stripping in symmetric cells with Ag@PDA@PCS-Li, PCS-Li and Li-foil electrodes cycled at (b) 1 mA/cm^2 (1 mAh/cm^2) and (c) 2 mA/cm^2 (1 mAh/cm^2). Cycling performance of full cells used (d) LFP and (e) NCM811 cathodes at 0.5 C.

shows other substrates such as coin, glass, and rubber materials are used as coating objects respectively, which is essential for practical applications in Li metal batteries.

In summary, we proposed a simple and effective strategy for constructing a congener-derived lithiophilic organic-inorganic interphase/layer on arbitrary collectors. After the initial lithium deposition, the stable congener-derived SEI with relatively minor inorganic components and more organic components is electrochemically formed. The inorganic components such as Li_2CO_3 and LiF on the surface are significantly less than those of the ordinary Cu foil, while the C–O–Li is more. The reasonable content of inorganic components could enhance the SEI layer, while too many inorganic components make the deposition of lithium ions more inhomogeneous. The stable congener-derived layer/interphase contains rigid inorganic components and flexible organic components, which provide flexibility and elasticity to stabilize the lithium metal anode during cycling. The strong interaction between Li^+ and o–dione of PDA induces uniform lithium deposition and Li^+ flux. In the embodiment, the submicron channel significantly restrained the volume expansion during the cycles and ensured the stability of the structure which allowed plenty of space for deposition and alleviates the dendrite problem. This strategy is also applied to the high-temperature carbonized rice paper film, which not only obtained ultra-high capacity density, but also has ultra-stable cycle stability and long life. This work provides a template method for preparing anodes with congener-derived interphase, which has the potential to realize the practical high-volumetric-capacities LMBs.

Declaration of competing interest

All authors declare that they have no known competing financial interests or personal relationships that could have appeared to influence the work reported in this paper.

Acknowledgments

This work was supported primarily by the National Natural Science Foundation of China (No. 22109025), National Key Research and Development Program of China (No. 2020YFA0710303), Natural Science Foundation of Fujian Province, China (No. 2021J05121).

Supplementary materials

Supplementary material associated with this article can be found, in the online version, at doi:10.1016/j.cclet.2023.108451.

References

[1] D. Lin, Y. Liu, Y. Cui, Nat. Nanotechnol. 12 (2017) 194–206.
[2] J.B. Goodenough, K.S. Park, J. Am. Chem. Soc. 135 (2013) 1167–1176.
[3] S. Li, M. Jiang, Y. Xie, et al., Adv. Mater. 30 (2018) 1706375.
[4] J.W. Choi, D. Aurbach, Nat. Rev. Mater. 1 (2016) 16013.
[5] G. Xu, R. Li, M. Li, et al., Chem. Eng. J. 434 (2022) 134498.
[6] N. Nitta, F. Wu, J.T. Lee, G. Yushin, Mater. Today 18 (2015) 252.
[7] R. Shao, C. Yang, C. Yang, et al., J. Energy Chem. 58 (2021) 280–284.
[8] W. Xu, J. Wang, et al., Energy Environ. Sci. 7 (2014) 513–537.
[9] P. Shi, L.P. Hou, C.B. Jin, et al., J. Am. Chem. Soc. 144 (2022) 212–218.
[10] Y.X. Zhan, P. Shi, X.X. Ma, et al., Adv. Energy Mater. 12 (2022) 2103291.
[11] Y. Zhang, J. Qian, W. Xu, et al., Nano Lett. 14 (2014) 6889–6896.
[12] Z. Li, J. Huang, Y.B. Liaw, et al., J. Power Sources 254 (2014) 168–182.
[13] K.H. Chen, K.N. Wood, E. Kazyak, et al., J. Mater. Chem. A. 5 (2017) 11671–11681.
[14] K. Xie, W. Wei, K. Yuan, et al., ACS Appl. Mater. Interfaces 8 (2016) 26091–26097.
[15] L. Lin, F. Liang, K. Zhang, et al., J. Mater. Chem. A 6 (2018) 15859–15867.
[16] X. Luan, C. Wang, C. Wang, et al., ACS Appl. Mater. Interfaces 12 (2020) 11265–11272.
[17] R. Li, J. Wang, L. Lin, et al., Mater. Today Energy 15 (2020) 100367.
[18] F. Liang, L. Lin, Z. Feng, et al., J. Mater. Chem. A 7 (2019) 8765–8770.
[19] B. Zhu, Y. Jin, X.Z. Hu, et al., Adv. Mater. 29 (2017) 1603755.
[20] G. Zheng, S.W. Lee, Z. Liang, et al., Nat. Nanotechnol. 9 (2014) 618–623.
[21] M.H. Ryou, Y.M. Lee, Y. Lee, M. Winter, P. Bieker, Adv. Funct. Mater. 25 (2015) 834–841.
[22] K. Yan, H.W. Lee, T. Gao, et al., Nano Lett. 14 (2014) 6016–6022.
[23] X. Zhang, Q. Zhang, X.G. Wang, et al., Angew. Chem. 130 (2018) 12996–13000.
[24] K. Xie K, K. Yuan, K. Zhang, et al., ACS Appl. Mater. Interfaces 9 (2017) 4605–4613.
[25] F. Ding, W. Xu, G.L. Graff, et al., J. Am. Chem. Soc. 135 (2013) 4450–4456.
[26] Q. Wang, C. Yang, J. Yang, et al., Adv. Mater. 31 (2019) 1903248.
[27] J. Guo, Y. Chen, Y. Xiao, et al., Chem. Eng. J. 422 (2021) 130526.
[28] M. Ge, X. Zhou, Y. Qin, et al., Chin. Chem. Lett. 33 (2022) 3894–3898.
[29] R. Zhang, X.B. Cheng, C.Z. Zhao, et al., Adv. Mater. 28 (2016) 2155–2162.
[30] X. Sun, C. Yang, Y. Zhao, et al., Adv. Funct. Mater. 32 (2022) 2109112.
[31] L. Wang, X. Zhu, Y. Guan, et al., Energy Stor. Mater. 11 (2018) 191–196.
[32] T. Zhou, Y. Mu, J. Wu, et al., Chin. Chem. Lett. 33 (2022) 2165–2170.

[33] B. Hong, H. Fan, X.B. Cheng, et al., Energy Stor. Mater. 16 (2019) 259–266.
[34] Y. He, H. Xu, J. Shi, et al., Energy Stor. Mater. 23 (2019) 418–426.
[35] K. Yan, Z. Lu, H.W. Lee, et al., Nat. Energy 1 (2016) 1–8.
[36] Y.W. Song, P. Shi, B.Q. Li, et al., Matter 4 (2021) 253–264.
[37] Q. Yun, Y.B. He, W. Lv, et al., Adv. Mater. 28 (2016) 6932–6939.
[38] H. Zhao, D. Lei, Y.B. He, et al., Adv. Energy Mater. 8 (19) (2018) 1800266.
[39] Q.H. iu, T. Tang, M. Asif, et al., Adv. Funct. Mater. 29 (2019) 1808468.
[40] D. Zhang, A. Dai, M. Wu, et al., ACS Energy Lett. 5 (2019) 180–186.
[41] R. Li, M. Li, Y. Chao, et al., Energy Storage Mater. 46 (2022) 605–612.
[42] A.I. Danilov, E.B. Molodkina, Y.M. Polukarov, Russ. J. Electrochem. 36 (2000) 1236–1244.
[43] Y. Liu, C. Tan, Z. Jia, et al., J. Cent. South Univ. (Sci. Technol.) 41 (2010) 144–149.
[44] H. Lee, S.M. Dellatore, W.M. Miller, et al., Science 318 (2007) 426–430.
[45] S. Hong, Y.S. Na, S. Choi, et al., Adv. Funct. Mater. 22 (2012) 4711–4717.